CrossMark

RESEARCH ARTICLE

A new method of dynamic and static stall detection using infrared thermography

A. D. Gardner[1] · C. C. Wolf[1] · M. Raffel[1]

Abstract A new method of detecting flow separation for static and pitching airfoils is described, with application to the generation of stall maps for helicopter rotors. An airfoil is heated using a lamp, and a high-speed infrared camera monitors the surface temperature. Subtracting consecutive images and performing a spatial standard deviation over a region of interest yields a single σ DIT value which is used to detect boundary layer separation on the airfoil. The data can be analysed to identify attached flow (low values of σ DIT) and separated flow (high values of σ DIT). Although appropriate filtering can significantly improve the signal-to-noise ratio, the method is robust regarding the exact method of analysis and the unfiltered data are sufficiently clear to be analysed without additional processing. For the test airfoil used, stall was measured up to a pitching frequency of 5 Hz, and signal-to-noise ratios indicate that it should be possible to measure stall for a pitching frequency of 20 Hz for a carbon-fibre surface with the thermal properties used.

1 Introduction

Due to the nature of the problem, all helicopter main rotors in forward flight have areas of separated flow. For high-speed forward flight or highly loaded manoeuvring flight, the area of separated flow expands, and the large dynamic loads associated with the stalled areas of the blade require a limitation of the flight envelope.

The investigation of helicopter blade stall involves the production of "stall maps" where the areas on the rotor disc which are stalled are geometrically described. These are currently most commonly produced by the investigation of pressure sensor data from sensors integrated into the rotor blades (Bousman 1998), but early investigations used rotating camera observations of tufts attached to an uninstrumented blade to produce the same result (Gustafson and Myers 1946). The technical complexity of instrumenting rotor blades has lead to the development of other methods of detecting stall for a wind tunnel test of a rotor, including using Particle Image Velocimetry (PIV) (Mulleners et al. 2012) and Pressure Sensitive Paint (PSP) (Disotell et al. 2014). PIV provides flow field data definitively proving stall for a single radial and azimuthal position, but without needing any treatment of the rotor blade. PSP provides pressure data on the surface of the rotor which can be correlated with stall and requires painting the rotor blade, but can be performed after manufacture for any instrumented or uninstrumented blade.

Infrared cameras have long been used for flow analysis, with the observations of Thomann and Frisk (1967) being the first published experiments. For a long time, the only applications were in hypersonic research due to the low sensitivity of the cameras available (Gartenberg and Roberts 1992). The first subsonic investigations by Bouchardy et al. (1983) used a measurement of the recovery temperature in transonic flow to measure boundary layer transition. The work of Quast (1987) extended the application range by using a heated wall to measure heat transfer rather than recovery temperature, thus significantly increasing the

✉ A. D. Gardner
  Tony.Gardner@dlr.de

  C. C. Wolf
  Christian.Wolf@dlr.de

  M. Raffel
  Markus.Raffel@dlr.de

[1] German Aerospace Center (DLR), Institute of Aerodynamics and Flow Technology, Bunsenstrasse 10, 37073 Göttingen, Germany

signal available for measurement. Quast measured boundary layer transition and the laminar separation bubble at the boundary between laminar and turbulent boundary layer flow. The use of infrared thermography to detect boundary layer separation is a standard technique in the wind tunnel, although few authors (Gartenberg and Roberts 1991; Mai et al. 2008) publish results from it due to the difficulty in analysing the results. Thin resistive heating films have since been used by a large number of groups including de Luca et al. (1990). They showed that when the flow is separated over a laminar separation bubble on a Göttingen 797 airfoil that the convective cooling is significantly reduced and a warm area of separated flow can be detected by using an infrared camera. Astarita and Cardone (2000) used the heated thin-foil method to investigate flow in a 108° sharp turn of a channel showing flow separation. An overview of some recent experiments separation and transition detection using these methods is given by Carlomagno and Cardone (2010). With the availability on the market of high-speed infrared cameras, they have been used for the detection of boundary layer transition in the rotating system where that would not previously have been possible due to the camera framing time, including on a helicopter hovering in ground effect (Richter and Schülein 2014).

This paper will detail a new method for detecting steady and unsteady flow separation on an airfoil by the analysis of infrared data, with the potential for generating stall maps of highly loaded rotors without the technical complexity and costs of installing pressure sensors in the rotor blades. An example of the usage on a rotor up to a flow Mach number of 0.3 can be found in Raffel et al. (2016). The method is based on image acquisition using the DIT method of Raffel et al. (2015) and the ensemble-averaging flow analysis of Gardner and Richter (2015). Previous authors have concentrated on infrared analysis of time-averaged (or static) flow separation using a steady average of the temperature (or infrared image intensity) directly. This allowed the detection of separation regions which were constant in time, and required some edge detection. This new method provides a stalled/unstalled indicator for a selected region, but analyses the time variation in the measurement and is applicable to a dynamically varying flow separation with high variation frequency. Analysing differences between consecutive infrared images using Differential Infrared Thermography (DIT) was applied by Raffel et al. (2015) to find dynamically varying transition positions in the rotating or non-rotating frames with infrared cameras. Raffel et al. also used the technique of using spotlights to heat the surface without needing to apply a resistive heating film. The accuracy of the boundary layer transition position detected using DIT has been verified using a comparison with hot-film transition data and pressure signal analysis (Richter et al. 2016), and this paper demonstrates the applicability to separated flows.

If nominally identical (or very similar) flow conditions are averaged, then the standard deviation (the differences between these flow conditions) is dominated by the effects of turbulent processes. Gardner and Richter (2015) have shown that this can be used to identify the position of boundary layer transition on an airfoil using pressure sensor data. Further, the pressure sensor data of Gardner and Richter showed a much larger peak in standard deviation associated with flow separation. This peak can be used to identify areas of flow separation for either a statically inclined airfoil or a dynamically pitching airfoil.

2 Experiment and description of method

The same DSA-9A airfoil as investigated by Richter et al. (2016) in the TWG transonic wind tunnel was installed in the "one metre wind tunnel in Göttingen" (1MG), a low speed, open test section wind tunnel with flow of 50 m/s ($M = 0.14$, $Re = 1.0 \times 10^6$), see Fig. 1. The airfoil was instrumented with a single set of 50 Kulite pressure transducers installed in a single cut under the surface of the airfoil centreline. Hot-film sensors were mounted along a second cut, but were not used for the current experiment. The tufts in Fig. 1 were used before the main experiments to quickly identify airfoil pitching motions where the flow stalled, but not used during the main experiment, and the airfoil used the end-plates shown, to improve the two-dimensionality of the flow. The airfoil is pitched sinusoidally around c/4 at $\alpha = 19° \pm 8°$ at $f = 2.5$ Hz (reduced frequency $k = \pi fc/v_\infty = 0.06$), and the pressure data were sampled at 8000 samples per pitching period for 100 periods. The pressure data are phase-averaged over all periods and the mean and standard deviation in C_P (σC_P) is found for each of the 8000 phase angles (i) by:
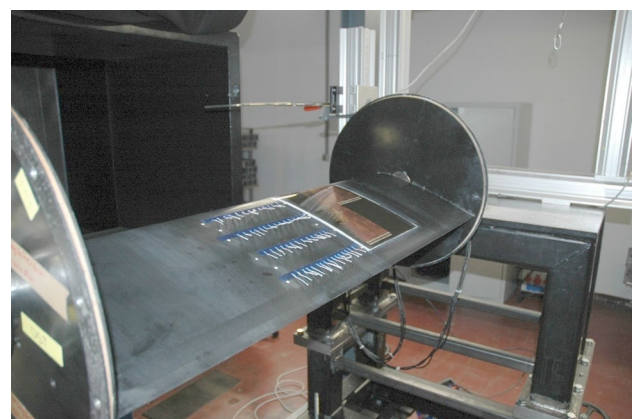

Fig. 1 DSA-9A airfoil installed in the 1MG open test section. Flow is from left to right. Pictured are hot-films on the airfoil surface and tufts for flow visualisation
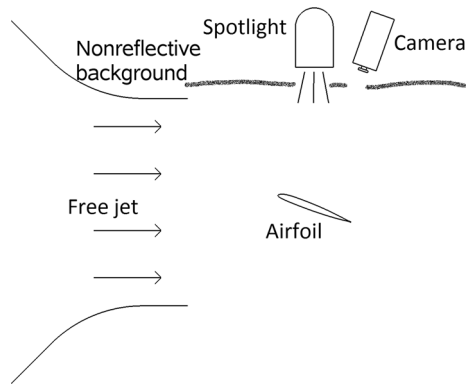
Fig. 2 Sketch of the experimental arrangement (*side view*)

$$\sigma C_{P_i} = \sqrt{\frac{1}{100} \sum_{n=1}^{100} \left(C_{P_{i+8000n}}^2 - \overline{C_{P_i}}^2 \right)}, \tag{1}$$

where

$$\overline{C_{P_i}} = \frac{1}{100} \sum_{n=1}^{100} C_{P_{i+8000n}}. \tag{2}$$

The set-up for DIT is shown in Fig. 2. The airfoil in the centre of the wind tunnel free-jet (static temperature 26 °C) is heated by a 2 kW lamp from 2 m above the airfoil, which was adjusted so that the central spot uniformly heated the area under observation. Under constant flow, the surface temperature was measured to be 37 ± 2 °C using a handheld infrared thermometer. A high-speed infrared (HSIR) camera (FLIR SC7750-L) was installed above the airfoil and observed the central part of the airfoil upper side. The HSIR camera had a spectral range of 8.0–9.4 µm detected by a Cadmium–Mercury–Telluride FPA detector with a resolution of 640×512 px. A 50-mm focal length lens with an aperture 2.0 was used. The data acquisition used an integration time of 200 µs, with an acquisition rate of $f = 107$ Hz. The camera was prepared using a two-point non-uniformity correction of the individual pixel sensitivity using a cold and hot hollow spherical half-shell held in front of the lens before each set of measurements. The DIT method evaluates intensity differences in the thermal images, and thus the conversion of intensity levels to temperature levels was not undertaken for the measurements. The camera measured noise equivalent temperature difference (NETD) was 35 mK at the temperatures used, and a single image intensity count was 8.4 mK at 26 °C up to 50 mK at 47 °C. Images were acquired using the "Altair" software. The output of the camera was monitored with the data acquisition system for the pressure and angle of attack sensors so that a synchronisation between the different systems could be achieved.

The surface properties of the airfoil have a significant effect on the infrared signal measured, as recently explored by Simon et al. (2016). The airfoil surface was made of carbon-fibre reinforced plastic with a black colour, with an estimated emissivity of $\epsilon = 0.95$ (Richter et al. 2016). An external layer of unreinforced resin was painted into the mould during manufacture, and this layer was polished after the airfoil was removed from the mould. The airfoil is made of two 3 mm shells (top and bottom) constructed using the L285/H287 system of the firm Hexion, and the fibre volume is 45 %. We do not have exact values for the thermal properties of the surface, but from the material data sheets estimate the thermal conductivity through the shell as $k_v = 0.5$ W/m/K and along the shell as $k_h = 7$ W/m/K, density $\rho = 1180$ kg/m^3 and specific heat capacity $Cp = 2300$ J/kg/K. Thus, the surface has low heat conductivity in the vertical direction. An important part of the set-up is the reduction in reflections, since small reflections have a large effect in the difference images. The reflections were reduced by observing the airfoil without flow and adjusting a black cloth (noted in Fig. 2) so that reflections were not seen.

Figure 3 shows a sample individual infrared image taken for flow at a static angle of attack. The flow in this image is from left to right, and the airfoil leading and trailing edges are visible. Boundary layer transition is visible as a light/dark boundary in the image as the surface heat flux changes over the transition region, and dark marker dots (conductive silver paint which was polished smooth) are also visible. At the top of the image, the edge of the hot-film foil (not used) is visible, and the pressure taps are in a single cut between the two rows of markers with the Kulite XQ093 sensors installed underneath the surface, as marked on the image. The pressure sensors have a small effect on the flow,
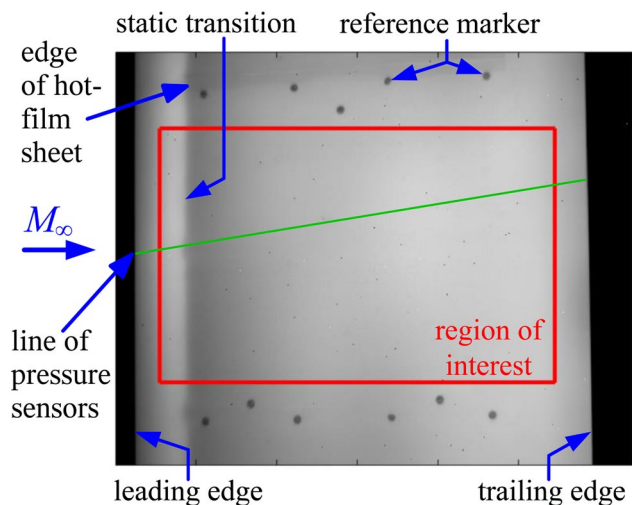

Fig. 3 Example static image showing the sampling area on the airfoil

visible in the slight wiggle in the transition position half-way between the dots, but the influence is not sufficient to cause transition to move significantly or the separation behaviour to change. Without flow or heating of the surface, a small temperature increase can be observed along this line due to the sensor excitation current, but this effect was not visible in the measurements in this paper. To perform the analysis of the separated flow on a pitching airfoil, 6000 infrared images were taken at 107 Hz, which amounts to data for 140 pitching cycles over 56 s of measurement time. The images were sorted into position along the cycle of the periodic movement, forming 300 bins in t/T. The data in each bin were then sorted in ascending time, so that the images nearest to each other were nearest in time and any effect of a temperature gradient over the measurement time would be reduced. Pairs of consecutive images were subtracted from each other to form $n-1$ DIT images in each bin of n IR images. Due to the relatively low frame rate of the camera compared to the pitching rate, pairs of "consecutive" images in the sorted data always came from different pitching cycles of the airfoil, thus the changes in the difference images indicate a shift from attached flow which is similar between different pitching cycles to separated flow which differs between pitching cycles.

An analysis window ("region of interest" in Fig. 3) was selected to avoid the edge effects of the airfoil and the reference markers. For the images in this paper, no mapping to compensate for the pitching motion was undertaken, since the maximum marker movement between α_{max} and α_{min} was 13 pixels, meaning that in each bin the maximum movement was <0.1 pixels. It was thus not felt that a mapping would improve the images. Experimentally it was shown that even when the number of bins was reduced to 75 that the signal-to-noise ratio did not increase, so it appears that the technique is not very sensitive to an exact mapping. Since no mapping was used, the dead/outlier pixels seen in Fig. 3 were also not compensated, but summed to zero during the differencing of two images for the DIT. The DIT images were then smoothed using a 3×3 pixel running average, which reduced the effect of pixel noise. For each DIT image, the spatial standard deviation was calculated over the analysis window, with the signal from each pixel contributing equally to the standard deviation. This yields a single σDIT value for each DIT image, which is related to the non-uniformity of the flow's thermal footprint. For each bin, the average spatial standard deviation was calculated, representing the combined information of 20 HSIR images in the case of dynamic pitching motions.

Variations on the evaluation method for the new images were tested and also found to work, as detailed later, but a reliable method for evaluating the images was:

1. Sort raw infrared images first by phase, then divide into bins and sort each bin in time.
2. Subtract consecutive images to form DIT images.
3. Smooth DIT images.
4. Define a spatial window.
5. Compute the spatial standard deviation over the window.
6. Average the standard deviation over each bin.

For the static flow, the number of bins is one, and a single standard deviation was acquired by averaging all 6000 IR images.

3 Static flow separation

For a statically inclined airfoil with flow at $v = 50$ m/s, example DIT images are shown in Fig. 4 for the sampling region indicated in Fig. 3. Here the pixel positions are approximately converted into positions on the airfoil (x/c, y/c) by a linear mapping. For the attached flow, the DIT images show almost zero signal, indicating that the flow is quite uniform and unchanging, and that the differencing correctly compensates for unevenness in the individual images due to inhomogeneous structure, lighting, surface heating or emissivity. The residual signal of about 2.0 is the image-to-image change in signal due to the airfoil vibration, changes in the wind tunnel flow, changes in temperature and lighting and sensor noise. In the DIT image for a statically inclined airfoil with separated flow, the difference between attached and separated flow is readily visible to the naked eye, since the 3D structures in the separated flow correlate poorly between consecutive images.

Fig. 4 Example images using the standard deviation of the DIT images **a** static, $\alpha = 10°$; **b** static, $\alpha = 28°$
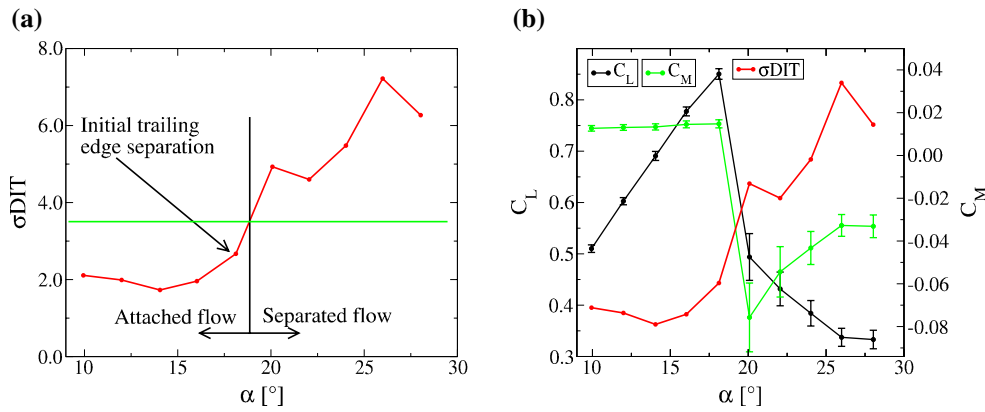
(a)

(b)
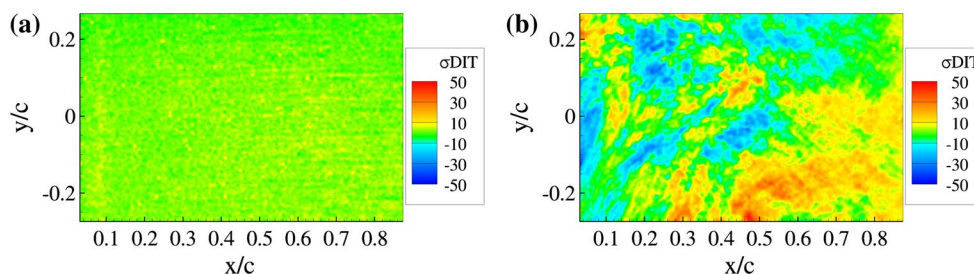
Fig. 5 **a** Variation of the standard deviation of the difference signal with phase for a static point. **b** Comparison of σDIT data with C_L and C_M polars.

If the σDIT values are plotted for a static polar, as seen in Fig. 5a, then a rise in σDIT is seen with the start of flow separation. The incipient start of trailing edge separation is seen as a small rise in σDIT from around 2 for attached flow ($\alpha < 16°$), and when σDIT is greater than around 4 ($\alpha > 20°$) then the flow is fully separated. The exact value of σDIT depends on the image quality, bin size and filtering used, and thus it is the rise from a constant value of σDIT during attached flow rather than the absolute value of σDIT which indicates flow separation. The comparison with the integrated pressure data for C_L and C_M shows that the initial rise in σDIT at $\alpha = 18°$ is due to the start of a trailing edge separation (seen in the change in gradient of C_L), and that the abrupt rise in σDIT at $\alpha = 20°$ is due to complete flow separation. Since the σDIT only gives a single value for the whole airfoil, flow separation can be assumed above the green line in Fig. 5a. Flow separation in the static case can also be easily shown using other methods, and thus it is the dynamic pitching case which will be investigated in more detail.

4 Detection of dynamic stall

For the dynamically pitching airfoil at $v = 50$ m/s, and $\alpha = 19° \pm 8°$ at $f = 2.5$ Hz, a dynamic stall condition is produced with generation of a leading edge dynamic stall vortex. The analysis of σDIT results in Fig. 6a, showing a region with low σDIT associated with attached flow and a region of high σDIT associated with separated flow. As a comparison, the standard deviation in C_P (σC_P) signal from a pressure sensor at $x/c = 0.10$ on the suction side of the airfoil is included. In the σC_P signal, the passage of boundary layer transition over the sensor can be seen at $t/T = 0.092$ (upstroke) and $t/T = 0.912$ (downstroke), and it can be seen that the large signal in σC_P due to flow
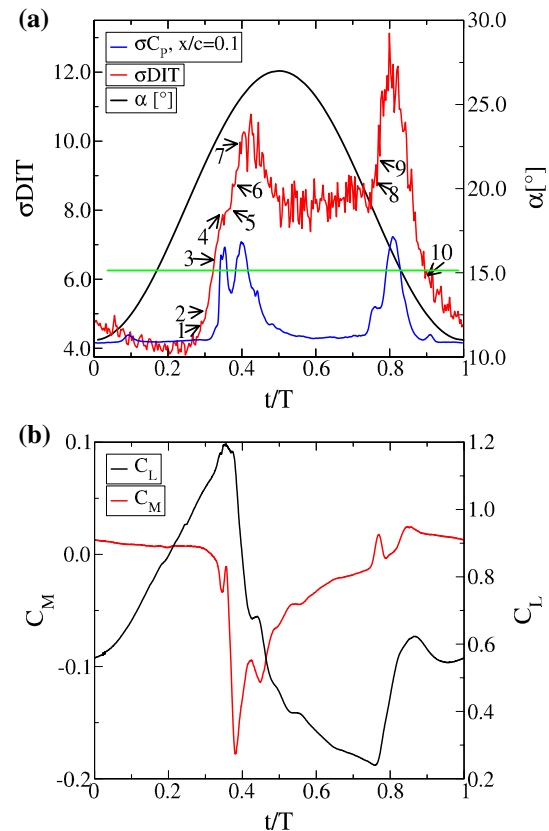
(a)

(b)

Fig. 6 Variation of signal with phase for a dynamic point **a** the standard deviation of the DIT images, averaged over the large window with 3×3 spatial smoothing using 300 bins over a cycle. **b** Phase-averaged lift and pitching moment integrated from the pressure sensors

separation is comparable both in time and shape to the σDIT signal. The gradients in σC_P at the start and end of stall are higher than seen in σDIT, and as will be seen later, this is an effect of the large spatial area used for the

σDIT signal. The fully separated flow shows a slightly increased level in σC_P compared to the attached flow. It is this effect which will be used in the DIT images to detect separated flow. The phase-averaged lift and pitching moments integrated from the pressure transducers (discretisation error $\ll 1$ %) are shown in Fig. 6b, showing a sudden stall and the generation of a large negative pitching moment peak.

Points from the pressure sensors could be used to identify particular points on the σDIT graph. For attached flow, σDIT is low, and for separated flow σDIT is high, with a cut-off between the two states around σDIT= 5, much higher than for the static case. From the analysis of the lift, pitching moment and pressure distributions, the following points could be clearly identified, as marked in Fig. 6:

1. Start of moment stall visible in C_M.
2. Start of the trailing edge separation visible in the pressure distribution.
3. Start of dynamic stall visible in the pressure distribution.
4. $C_{L_{max}}$.
5. Dynamic stall vortex generated starts to move downstream.
6. $C_{M_{min}}$.
7. Dynamic stall vortex over the airfoil trailing edge.
8. $C_{L_{min}}$.
9. Start of flow reattachment visible in the pressure distribution.
10. Flow reattachment complete visible in the pressure distribution.

The points 2, 3, 5, 7, 9 and 10 are extracted from the pressure distributions shown in Fig. 7, and the points 1, 4, 6, 7 and 8 are from the integral forces in Fig. 6b. The positions of the dynamic stall vortex are not always obvious from the individual points in Fig. 7 (see point 7 especially), but an analysis of the motion of the wave associated with the dynamic stall vortex allows its position to be clearly determined. The rising flank of the σDIT signal encompasses the whole dynamic stall process with the generation and convection of the dynamic stall vortex from the airfoil. The plateau in the middle of the peak is the region of fully separated flow, analogous to separated flow for a static airfoil. The flow reattachment starts at the rising flank of the second peak and continues until σDIT has dropped to the low level associated with attached flow.

The analysis of σDIT can thus give an indication of whether the flow on an airfoil is stalled. By setting a trigger level about halfway up the rising flank of σDIT, as for the green line in Fig. 6a, it can be indicated that all points which have σDIT above this have fully stalled flow on the airfoil. It can be seen from Fig. 6a that this will result in a temporal error in the detection of stall of around $\pm \Delta t/T = 0.025$.

A contrast to the analysis using the DIT can be found by investigating the mean value of the original images over the region of interest in Fig. 3. For the static test case, the temperature of the airfoil would be higher with separated flow as noted by many authors (Gartenberg and Roberts 1992; Carlomagno and Cardone 2010). For the dynamically pitching airfoil, the temperature does not reach a steady state, but the temperature increases when the flow is separated due to the reduced cooling from the airflow, see the mean temperature over the region of interest shown in Fig. 8. It can be seen that as soon as the flow stalls ($t/T = 0.35$), that the mean temperature has a positive gradient. At the point of reattachment ($t/T = 0.8$), the cooling due to the flow is reasserted and the surface cools until it reaches equilibrium at $t/T = 0.1$, whereafter the surface has a constant temperature until $t/T = 0.3$. At this point a higher heat transfer than in the attached flow is present, causing the surface temperature to reduce. This higher heat transfer is associated with the region of dynamic stall, as seen by the falling flank of C_M in Fig. 6b and the rising flank of σDIT in Fig. 6a and is related to the expansion of the trailing edge stall upstream, but the exact mechanism is not known at this time. Thus, the analysis of stall in the dynamic system is also possible using the mean temperature, but since different parts of the stall process result in either a higher or lower cooling of the surface than the attached flow, neither a peak analysis nor a gradient analysis would allow a good determination of the times of separation. For this reason, the analysis of σDIT is preferred as being simpler. As will be shown in the next section, the analysis of σDIT is also a robust and practical technique which is relatively insensitive to the exact algorithm used for the analysis.

5 Sensitivity analysis

The algorithms used to produce the σDIT values are investigated in this section to show the sensitivity of the process to changes in the analysis method. The smoothing, sorting and binning, and temperature differences can all be analysed for their optimal settings. Additionally, the effect of pitching frequency is shown to be uncritical.

Smoothing is used to improve the signal-to-noise ratio of the σDIT result. The effect of camera pixel noise can be reduced by either a spatial or a time smoothing, and a spatial filtering to remove small-scale structures and prefer large-scale structures selects more strongly for the difference between attached and separated flow. Figure 9 shows the use of spatial smoothing to improve the signal-to-noise ratio by averaging all of the original data in an NxN square onto the pixel in the middle of the square for the smoothed
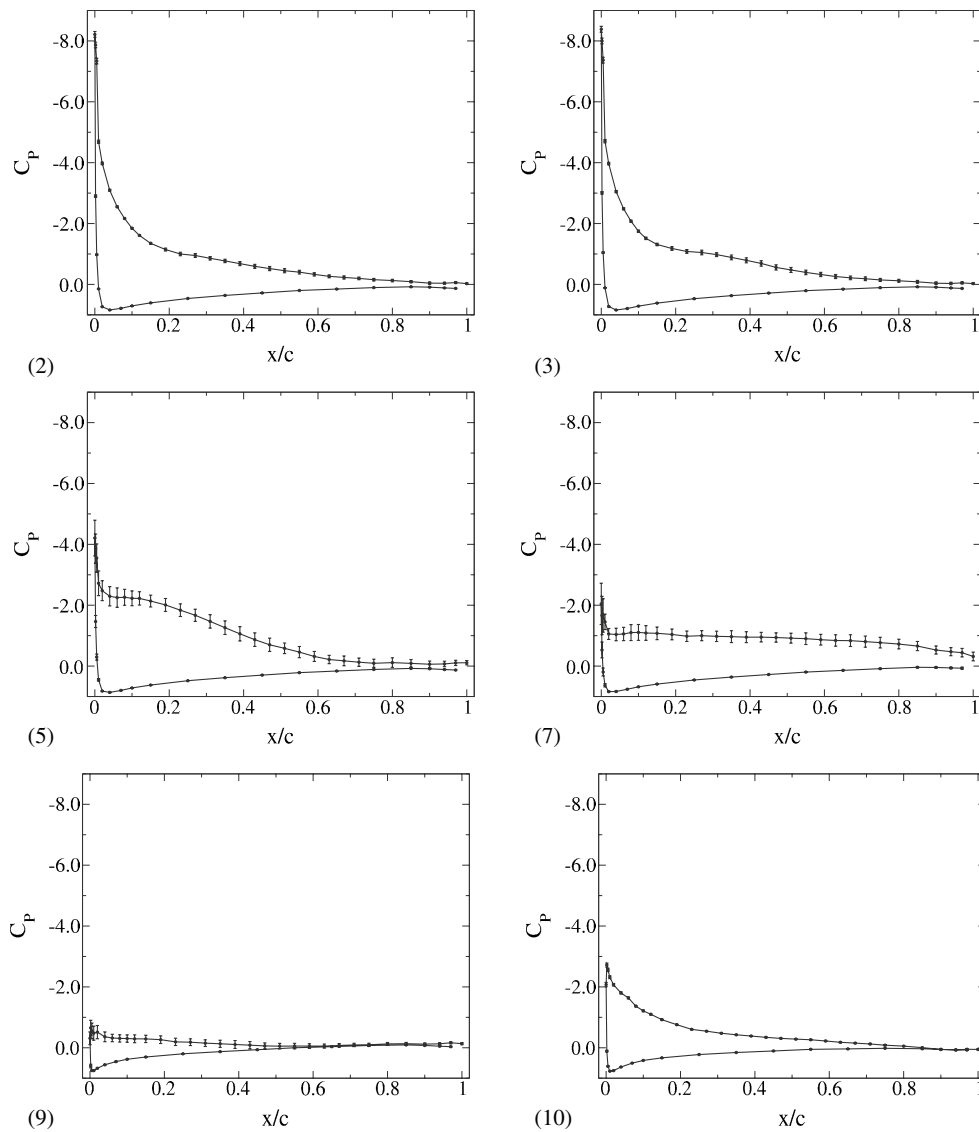
Fig. 7 Phase-averaged pressure distributions with standard deviations corresponding to the points in Fig. 6
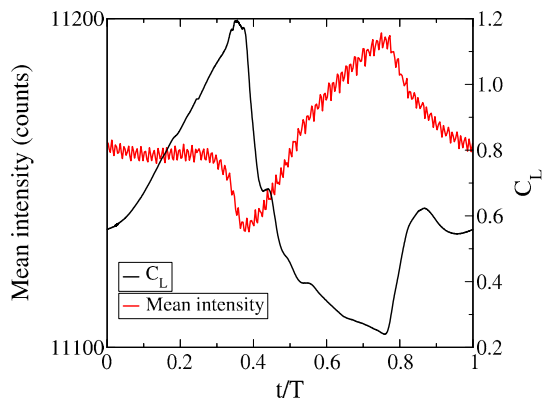

Fig. 8 Variation of the mean over the sampling window of the original infrared images, averaged over the large window with 3×3 spatial smoothing using 300 bins over a cycle.
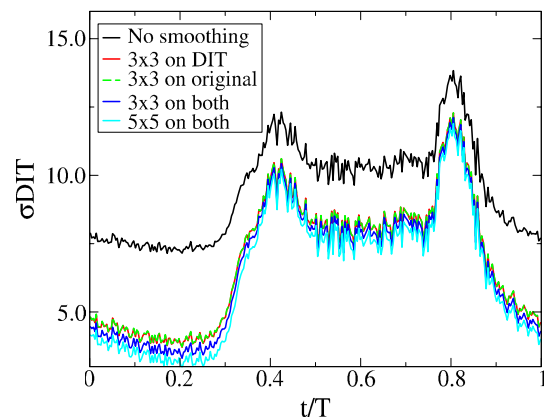

Fig. 9 Comparison of σDIT for different spatial smoothing schemes using 300 bins over a cycle

data. Without smoothing, the black line has a signal-to-noise ratio (SN) of SN = 1.8, if we divide the highest peak by the deepest trough after a 10-point moving average. Using the same method on the 3×3 pixel smoothing, it can be seen that the signal-to-noise ratio increases to SN = 3.0, regardless of whether the smoothing is performed on the original images or on the DIT data. Smoothing on both data sets improves the signal-to-noise ratio only marginally to SN = 3.3. Using a larger 5×5 window improves the signal-to-noise ratio again to SN = 3.6, but it can be seen that the main improvement was already in the original 3×3 smoothing. Thus, for the investigations of other effects, the 3×3 smoothing on the DIT data will be used to provide a constant reference point.

A second option for the smoothing is to smooth over time, where the results for a single pixel are smoothed using a moving average in time with a width of ± 5 time steps. The results of this smoothing are seen in Fig. 10. If the smoothing is performed on the original data, it is ineffective in improving the signal-to-noise ratio and greatly reduces the absolute value of σDIT, since the differences between consecutive images are reduced, and the DIT is rendered ineffective. The result also suffers from quantization effects, since the differences between the two images are often less than one intensity count. If the time smoothing is performed after the image differencing is performed, a similar result to that for the 3×3 spatial smoothing is achieved with a signal-to-noise ratio of SN = 2.7 produced. This indicates that the primary effect of the 3×3 spatial smoothing is a reduction in the pixel noise from the camera rather than a spatial filtering.

The investigations above were performed with 300 bins of images per cycle, sorted with a phase/time sort. This means that the data are first sorted by phase, and then the phase space divided into N bins. Each bin is then sorted in time. The hope was that the slow change in surface temperature over time would be best compensated by this method. Figure 11 shows the increase in temperature over time in infrared intensity counts for the single lamp used for the majority of tests. In this case, an intensity increase of 12 counts over the test time of 56 s was seen. As seen in Fig. 8, the absolute intensity is around 11000 counts, so this represents a change of around 0.1 %. As an alternative, a second lamp was additionally used to heat the airfoil and this resulted in an increase in temperature of 21 intensity counts over the test time. The surface temperature was measured to be $47 \pm 2\,^{\circ}$C using a hand-held infrared thermometer. As seen in Fig. 12, using the phase and time sort does result in a slight improvement in the signal-to-noise ratio over the simple phase sort for the case using two lamps (the signal-to-noise ratio increases from 3.0 to 3.1), thus for test cases where a significant change in temperature is expected over the test time the phase/time sorting is recommended, and
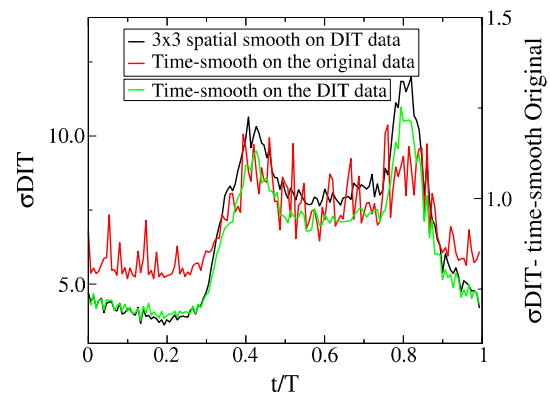

Fig. 10 Comparison of σDIT for time based and 3×3 spatial smoothing using 300 bins over a cycle
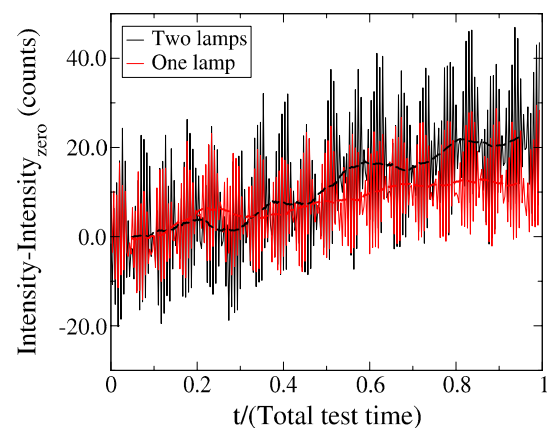

Fig. 11 Temperature rise as IR camera intensity counts over the test time for two different heating cases. *Thick lines* are running averages
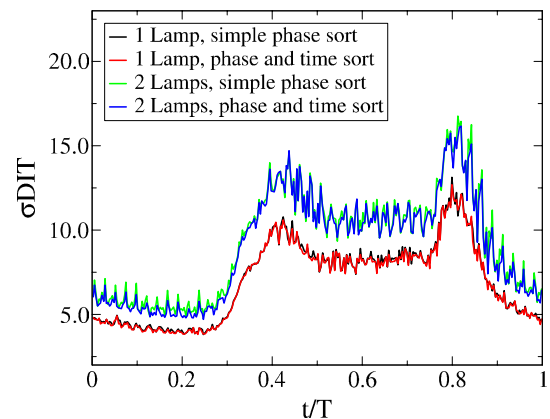

Fig. 12 Comparison of a simple phase sort and a phase/time sort. Comparison of different heating schemes, all with 3×3 spatial smoothing using 300 bins over a cycle

is used for all the reference cases in this paper. The signal-to-noise ratio is not improved by the additional heating of the second lamp, but the average temperature increase of
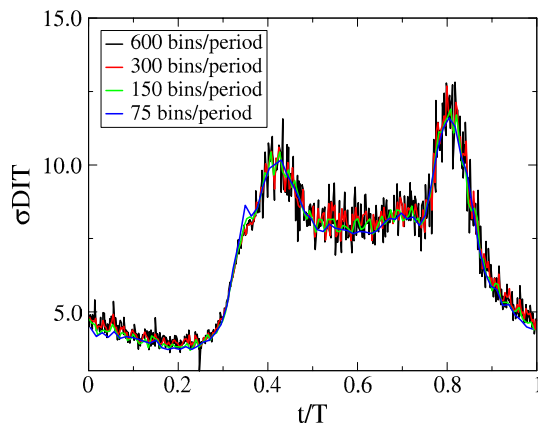
Fig. 13 Comparison of the effect of varying the number of bins per cycle with 3×3 spatial smoothing and a phase/time sort
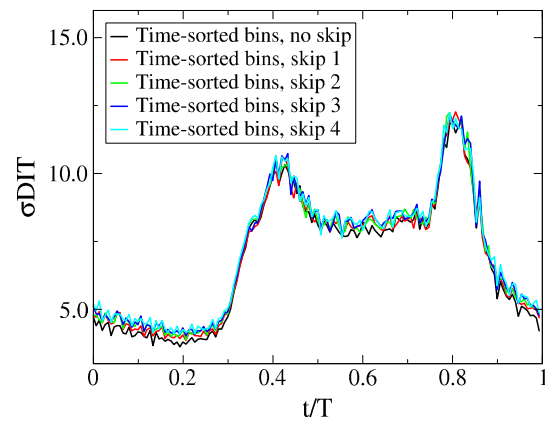

Fig. 14 Effect of increasing the time difference between original images used to form DIT images, where the original images are sorted into 150 bins per period

10 C meant that the average camera signal in the field of interest increased from 11200 to 11700 counts ($+4.5$ %). In principle, higher surface temperatures lead to less stability of the boundary layer, although the effect is not measurable in this case, as the separation angle was compared for test points with and without heating. For this test, the pressure data and infrared data were both acquired for the heated airfoil and no comparison was made to the cooler airfoil. Where a comparison with the cold airfoil is required, the level of heating should be limited. Costantini et al. (2015) estimate the acceptable overheat as between 1 % (to match transition position) and 10 % (to match lift), for a laminar airfoil with Reynolds number $4.5 \times 10^6 \leq Re \leq 13 \times 10^6$ (between 3 and 30 K at 300 K).

Choosing the phase/time sort for further investigations, the effect of varying the number of bins per period is shown in Fig. 13. It can be seen that the main effect is the same as if a running mean or low-pass filter was passed over the data. Since the image movement is not corrected, the maximal pixel movement increases from 0.04 pixels/bin for the case using 600 bins to 0.35 pixels/bin for the case using only 75 bins, which is still around the residual movement remaining after using a derotation algorithm. The effect of alignment errors can be further investigated by sorting the data into 150 bins and changing the time between images used to form the DIT images, thus increasing the movement between DIT images. This method is shown in Fig. 14 for no skipping (reference) and skipping 1, 2, 3 and 4 intermediate images between the images used to form the DIT image. It can be seen that a small effect is present, reducing the signal-to-noise ratio from SN = 3.0 to SN = 2.9 for the worst case, but the total effect is small. In general, it can be posited that the alignment does not have a critical effect on the computation of σDIT, but that a gradual reduction in the signal-to-noise ratio should be expected with increasing alignment divergence between the two images used for the DIT.
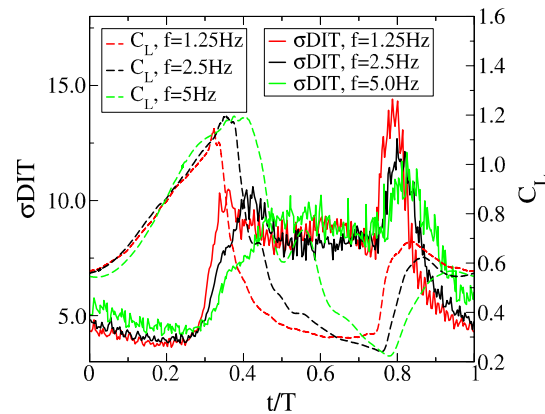

Fig. 15 Comparison of the measurement with different pitching frequencies, averaged over the large window with 3×3 spatial smoothing using 300 bins over a cycle

Increasing the airfoil pitching frequency at constant flow speed increases the reduced pitching frequency from $f = 1.25$ Hz ($k = 0.03$) through $f = 2.5$ Hz ($k = 0.06$) to $f = 5$ Hz ($k = 0.12$). As seen in Fig. 15, increasing the pitching frequency delays the dynamic stall to higher angles of attack, and makes the dynamic stall process shorter in absolute time but longer in t/T. The higher pitching frequencies also have higher lift before stall, meaning that more circulation is available to be entrained into the dynamic stall vortex. The flow reattachment is at around the same phase for each of the three pitching frequencies investigated. The infrared images are taken at the same rate (107 Hz) for each of the three frequencies, and for each case 6000 images are taken. The 6000 images are then sorted along the phase, so that the normalised time ($\Delta t/T$) between images is the same. The σDIT signals show the slowing of the stall process as seen in the

lift curves. The σDIT curves are more smoothed at higher frequencies, with the peaks reduced and the base level of σDIT increasing.

When the pitching frequency of the airfoil is changed, this also has an effect on the σDIT. Since the infrared camera frequency and number of images remain constant, the number of infrared images remains constant, and thus there is not a loss in the resolution with which the pitching cycle is resolved. Despite this, the signal-to-noise ratio is worse for higher pitching frequencies (Fig. 15). At the limit of very high pitching frequencies, it is clear that the airfoil surface would take on a constant temperature distribution and no signal would result, so increasing the pitching frequency will tend to reduce the signal. A constant trend of reduction in signal-to-noise ratio is visible from $f = 1.25$ Hz (SN = 3.6) through $f = 2.5$ Hz (SN = 3.0) to $f = 5.0$ Hz (SN = 2.5). Assuming this trend continues, the signal-to-noise ratio at 20 Hz should be still good at around SN = 1.3–1.5, or good measurement values up to a reduced frequency of $k = \pi f c / v_\infty = 0.038$ for this carbon-fibre surface. The effect of pitching frequency will be dependant on the thermal conductivity and heat capacity of the surface, with more insulating surfaces still being good to higher frequencies.

6 Effect of interrogation windows

In the classic stall map using tufts, the separation at each tuft can be analysed to give a map of where on the blade at each instant the flow is stalled. Figure 16 shows that for smaller squares, it can be seen that the signal-to-noise ratio is reduced from SN = 3.0 to SN = 2.8 for the 100×100 px square and to SN = 2.3 for the 50×50 px square. Using such squares indicates how the signal-to-noise ratio becomes worse though insufficient camera resolution, which is always a problem when using infrared cameras on rotors. It can also be seen that the smaller windows deliver more local information, which can be seen in the steeper gradient in σDIT during stall. This opens the possibility of using a moving window technique to analyse the data, so that a surface map of separated/attached flow is generated.

The classical stall map requires knowing whether the rotor blade is stalled or not for each azimuthal angle and radial position. As such it is interesting to know how a thin slot-shaped window can be used to evaluate the flow state at different radii. Figure 17 shows the effect of reducing the width of the interrogation window while the length remains the same. Reducing the slot width from 315 pixels to 10 pixels reduces the signal-to-noise ratio slightly (From SN = 3.0 to SN = 2.9), but the difference is minimal. A classical stall map should then be no problem. Ordering the windows in slots normal to the flow direction, as in Fig. 18
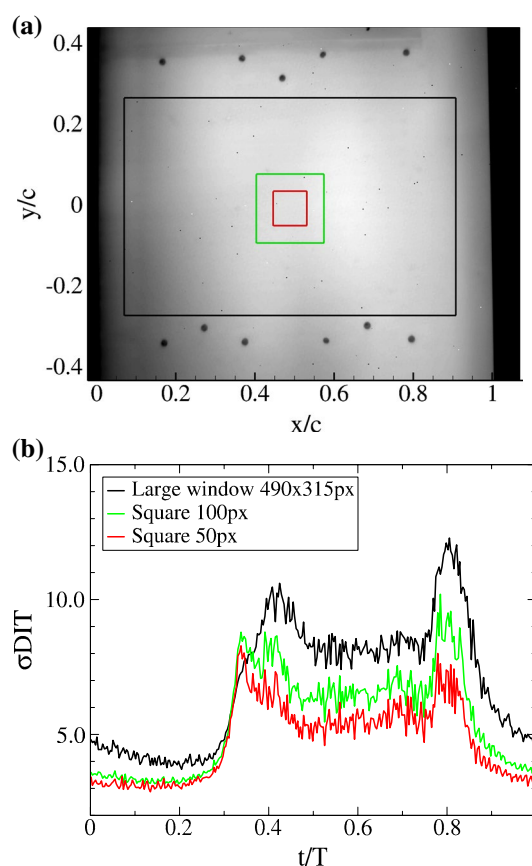

Fig. 16 For the square-shaped windows in (**a**), in (**b**) the variation of the σDIT with 3×3 spatial smoothing using 300 bins over a cycle

makes the progression of the stall from trailing edge to leading edge visible. The flow stalls first near the trailing edge in the cyan and blue windows, and last in the black window near the leading edge. A progression in the flow reattachment is also visible, with the black window reattaching first and the reattachment progressing downstream until the cyan window reattaches last. Using this type of slots generates a better signal-to-noise ratio than for the 50×50 px window (SN = 3.1 for the blue window compared to SN = 2.3 for the 50×50 px window), probably due to including three times as many pixels in the averaging window.

Using the slot interrogation window allows for a direct comparison between σDIT and σC_P data at the same location, as seen in Fig. 19. It can be seen that, in contrast to the differences in the rise and fall times seen in Fig. 6a, when the local σDIT is compared that the results are very similar. Both the start and end of dynamic stall are detected at the same point using both techniques, but the plateau during stall is significantly higher for σDIT than for σC_P. Although in this analysis the boundary layer transition was not detected using the IR data, a standard DIT analysis as applied by applied by Raffel et al. (2015) will produce the transition positions.
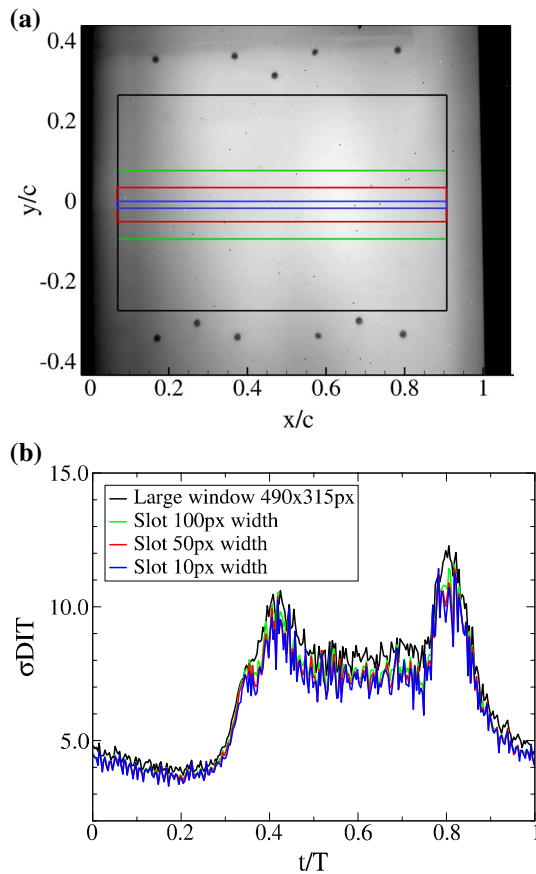
Fig. 17 For the slot-shaped windows in (**a**), in (**b**) the variation of the σDIT with 3×3 spatial smoothing using 300 bins over a cycle

Fig. 18 For the slot-shaped windows of width 25 pixels normal to the flow direction in (**a**), in (**b**) the variation of the σDIT with 3×3 spatial smoothing using 300 bins over a cycle

The 50×50 px window can be moved over the image, to provide a spatial evaluation of the DIT images. The windows were moved in steps of 25 px for an overlap in both the x and y directions of 50 %. The σDIT images generated in this way can be seen in Fig. 20 to fill a portion of the original image. In Fig. 20, the flow is attached at $t/T = 0.25$, just before the start of flow separation (Compare with Fig. 6). The value of σDIT is not constant over the image, but at all times σDIT < 4. Examining the separation and reattachment processes in Fig. 21 shows that at $t/T = 0.30$ (Fig. 21a), the separated flow is moving from the top right to the bottom left of the image. The airfoil centreline is at around the top of the raw image, and for an airfoil with free ends, the flow will separate first on the airfoil centreline since the effective angle of attack of the airfoil is highest on the centreline and reduces in an elliptical distribution towards the free ends of the airfoil. The movement of the separated flow from trailing edge to leading edge is also noted in the pressure distributions in Fig. 7.

As the trailing edge separation advances towards the leading edge a point is reached where the airfoil is separated, but the suction peak is still preserved. This is seen in pressure
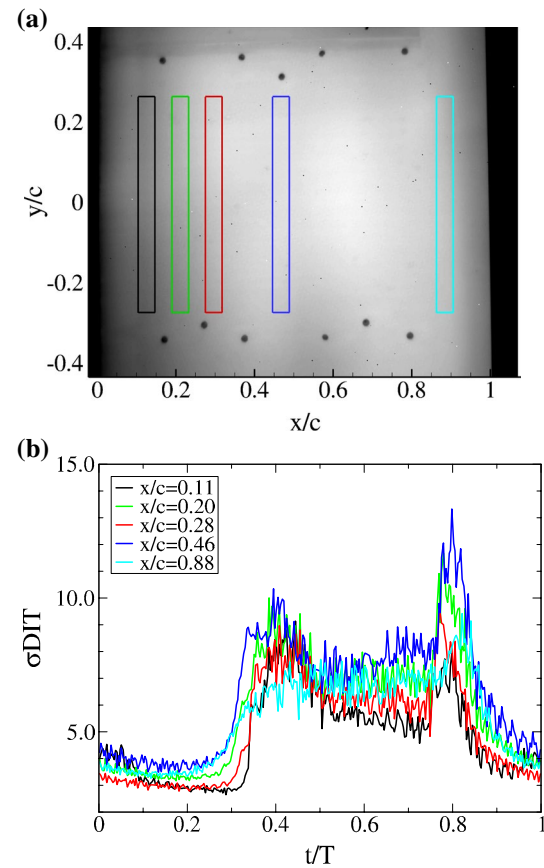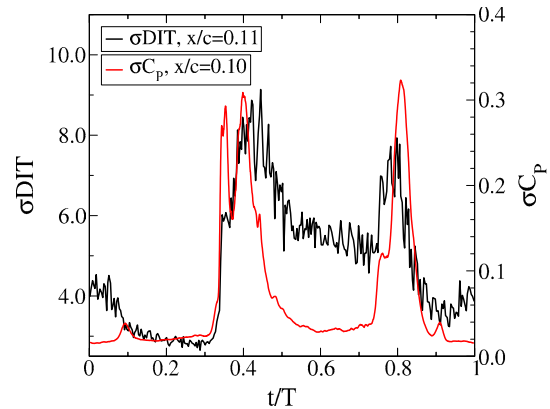

Fig. 19 Comparison of σDIT and σC_P at the same location

distribution (2) in Fig. 7, and in Fig. 21b. The movement of the trailing edge separation pauses from $t/T = 0.32$ to $t/T = 0.34$ before continuing upstream. By $t/T = 0.35$, shown in Fig. 21c, σDIT > 5 over the whole airfoil. As seen in Fig. 6, this time is where the slight plateau in σDIT was observed for the whole airfoil. The pressure distributions indicate that this is when the
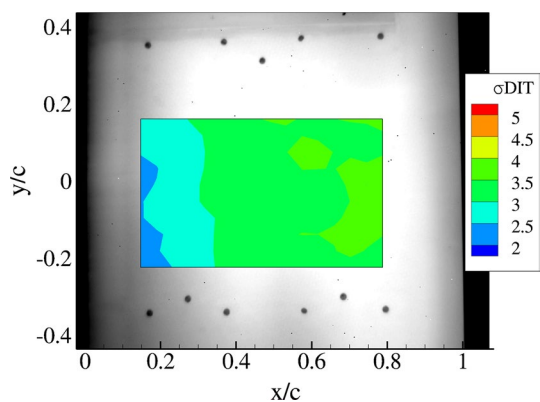
Fig. 20 Data from the moving 50×50 px window with 25 px overlap at $t/T = 0.25$ showing the position of the data window

leading edge dynamic stall vortex is formed and starts to propagate downstream. The images with the moving window after $t/T = 0.35$ do not show the motion of the dynamic stall vortex, but remain at a high level of σ DIT. After the dynamic stall process, the airfoil presents fully stalled flow which is similar to that seen for the static stall case, and Fig. 21d shows a similar non-uniform σ DIT distribution to that seen for the attached flow, but with a mean level of around σ DIT $= 4.5$. This situation remains until the start of the reattachment process.

Figure 21e shows the early phase of the reattachment process at $t/T = 0.83$, with reattaching flow moving

from the leading edge to the trailing edge. This process is also visible in an analysis of the pressure sensor data (not shown), as the suction peak reestablishes before the flow at the trailing edge is reattached. The final snapshot in Fig. 21f shows the progress of the flow reattachment at $t/T = 0.856$, and by $t/T = 0.88$ the flow is reattached and the σ DIT image is again similar to that for the attached flow in Fig. 20. The method of using a moving evaluation window is a powerful analysis technique showing the spatial separation and reattachment processes on the airfoil. The technique depends on having sufficient pixels in the evaluation window to increase the signal-to-noise ratio to an acceptable level. It can be envisaged that in the future with high-resolution IR cameras that the moving window method will be a practical technique for wind tunnel analysis. Where lower numbers of pixels are available, the single window evaluation method will probably be preferable.

7 Conclusion

A new method of detecting flow separation for static and pitching airfoils is described. The method is robust and does not require contact with the surface, any kind of surface treatment or instrumentation and can produce maps of the surface on which stalled and unstalled areas are detailed. The important results are:

Fig. 21 Data from the moving 50×50 px window: **a** $t/T = 0.30$, **b** $t/T = 0.32$, **c** $t/T = 0.35$, **d** $t/T = 0.50$, **e** $t/T = 0.83$, **f** $t/T = 0.856$
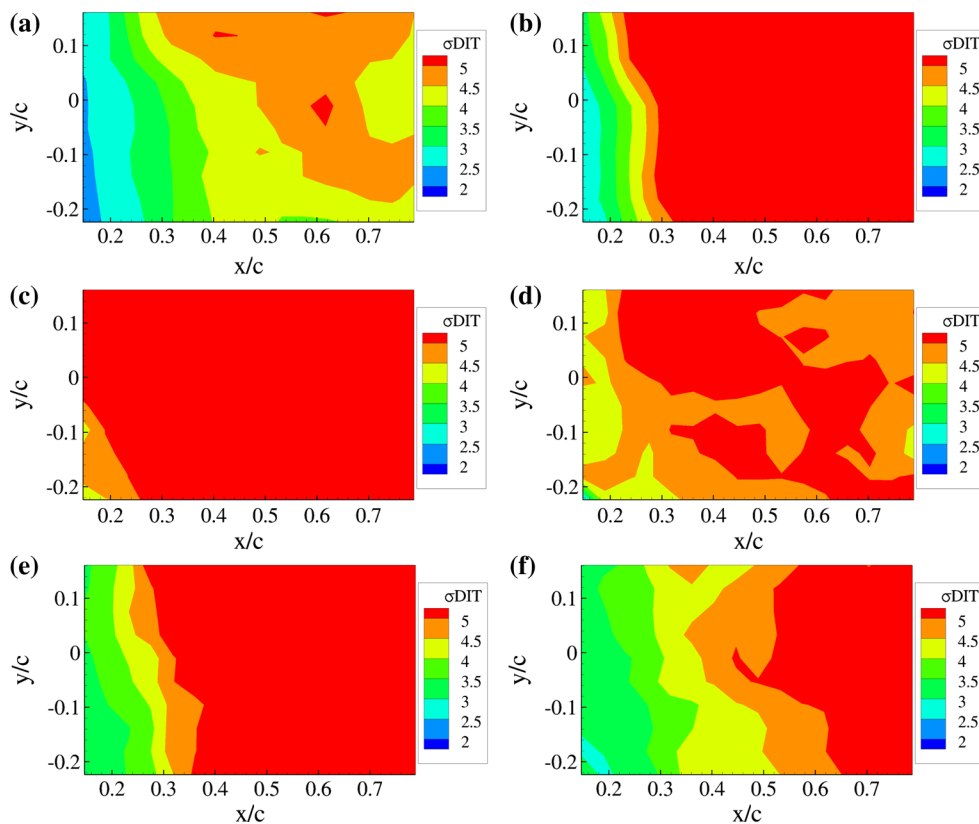
- A high-speed infrared camera is used and then difference images (DIT) between consecutive images are formed. A cut-out window is defined, and in that window, the standard deviation is computed to form a single value, σDIT.

- σDIT is high for separated flow and low for attached flow and this could be verified by comparison with unsteady pressure distributions.

- The paper describes methods of enhancing the signal-to-noise ratio of the images using filtering, sorting and window selection methods, and the signal-to-noise ratio could be improved to SN = 3.6; however, even the unfiltered data had a signal-to-noise ratio of 1.8, which is usable.

- The method works both for a statically inclined airfoil and a pitching airfoil which was tested up to a pitching frequency of 5 Hz. Extrapolations suggest that data could be extracted from the airfoil tested at least up to 20 Hz, but this value will be dependant on the thermal properties of the airfoil surface. Selecting surfaces with lower thermal response times as done by Simon et al. (2016) should result in an increase in signal-to-noise ratio and the upper limit of the pitching frequency.

- Using a moving window produced spatially resolved stall maps of the surface which could be verified by comparison with pressure distributions.

Where pressure or heat flux measurements are unavailable, the analysis of σDIT provides a binary stalled/unstalled indication for areas on a wing. In contrast with pressure measurements, a measurement of the whole surface can be achieved without requiring the installation of sensors or surface preparation. However, the analysis of pressure or heat flux signals gives more details about the stall process, when available. This new use for highly resolving and fast IR cameras in aerodynamic research has also been tested for a rotating dynamically pitching airfoil in the rotor test stand (RTG) of the DLR in Göttingen (Schwermer et al. 2016) up to Mach 0.3, with encouraging initial results, as shown by Raffel et al. (2016).

References

Astarita T, Cardone G (2000) Thermofluidynamic analysis of the flow in a sharp 180 degrees turn channel. Exp Therm Fluid Sci 20(3–4):188–200. doi:10.1016/S0894-1777(99)00045-X

Bouchardy A-M, Durand G, Gauffre G (1983) Processing of infrared thermal images for aerodynamic research. Appl Digital Image Process 397:304–309. doi:10.1117/12.935316

Bousman WG (1998) A qualitative examination of dynamic stall from flight test data. J Am Helicopter Soc 43(4):279–295. doi:10.4050/JAHS.53.26

Carlomagno GM, Cardone G (2010) Infrared thermography for convective heat transfer measurements. Exp Fluids 49(6):1187–1218. doi:10.1007/s00348-010-0912-2

Costantini M, Fey U, Henne U, Klein C (2015) Influence of non-adiabatic model surface on transition measurements using the temperature-sensitive paint technique in a cryogenic wind tunnel. AIAA J 53(5):1172–1187. doi:10.2514/1.J053155

de Luca L, Carlomagno GM, Buresti G (1990) Boundary-layer diagnostics by means of an infrared scanning radiometer. Exp Fluids 9(3):121–128. doi:10.1007/BF00187411

Disotell KJ, Peng D, Juliano TJ, Gregory JW, Crafton JW, Komerath NM (2014) Single-shot temperature- and pressure-sensitive paint measurements on an unsteady helicopter blade. Exp Fluids. doi:10.1007/s00348-014-1671-2

Gardner AD, Richter K (2015) Boundary layer transition determination for periodic and static flows using phase-averaged pressure data. Exp Fluids. doi:10.1007/s00348-015-1992-9

Gartenberg E, Roberts AS (1991) Airfoil transition and separation studies using an infrared imaging system. J Aircr 28(4):225–230. doi:10.2514/3.46016

Gartenberg E, Roberts AS Jr (1992) Twenty-five years of aerodynamic research with infrared imaging. J Aircr 29(2):161–171. doi:10.2514/3.46140

Gustafson FB, Myers GC Jr (1946) Stalling of Helicopter Blades. In: NACA Report No. 840

Mai H, Dietz G, Geissler W, Richter K, Bosbach J, Richard H, de Groot K (2008) Dynamic stall control by leading edge vortex generators. J Am Helicopter Soc 53(1):26–36. doi:10.4050/JAHS.53.26

Mulleners K, Kindler K, Raffel M (2012) Dynamic stall on a fully equipped helicopter model. Aerosp Sci Technol 19:72–76. doi:10.1016/j.ast.2011.03.013

Quast A (1987) Detection of Transition by Infrared Image Technique. In: 12th international congress on instrumentation in aerospace simulation facilities (ICIASF 87), Williamsburg, VA, 22–25 June 1987, pp 125–134

Raffel M, Merz CB, Schwermer T, Richter K (2015) Differential infrared thermography for boundary layer transition detection on pitching rotor blade models. Exp Fluids. doi:10.1007/s00348-015-1905-y

Raffel M, Gardner AD, Schwermer T, Merz CB, Weiss A, Braukmann J, Wolf, CC, Ewers B (2016) Differential Infrared Thermography (DIT) for Dynamic Stall Detection. In: 18th International Symposium on Applications of Laser Techniques to Fluid Mechanics Lisbon, Portugal, 04–07 July, 2016

Richter K, Schülein S (2014) Boundary-layer transition measurements on hovering helicopter rotors by infrared thermography. Exp Fluids. doi:10.1007/s00348-014-1755-z

Richter K, Wolf CC, Gardner AD, Merz CB (2016) Detection of Unsteady Boundary Layer Transition Using Three Experimental Methods. In: 54th AIAA Aerospace Sciences Meeting, San Diego (CA), USA, 4–8 Jan 2016, AIAA-2016-1072. doi:10.2514/6.2016-1072

Schwermer T, Richter K, Raffel M (2016) Development of a rotor test facility for the investigation of dynamic stall. In: New results in numerical and experimental fluid mechanics X, notes on numerical fluid mechanics and multidisciplinary design, vol 132, pp 663–673. doi:10.1007/978-3-319-27279-5_58

Simon B, Filius A, Tropea C, Grundmann S (2016) IR thermography for dynamic detection of laminar-turbulent transition. Exp Fluids. doi:10.1007/s00348-016-2178-9

Thomann H, Frisk B (1967) Measurement of heat transfer with an infrared camera. Int J Heat Mass Transf 11:819–826. doi:10.1016/0017-9310(68)90126-9